ACTIVE WARPING CONTROL OF A JOINED-WING AIRPLANE CONFIGURATION

Carlos E. S. Cesnik*
University of Michigan, Ann Arbor, Michigan
and
Eric L. Brown†
Massachusetts Institute of Technology, Cambridge, Massachusetts

Abstract

This paper assesses the use of existing piezoelectric material technology for induced strain and producing wing-warping control on joined-wing aircraft configurations. Anisotropic piezocomposite actuators integrated into the wing structure are the method of actuation. Comparisons are made with traditional aileron control surface. This study is conducted based on a proposed framework in which the developed formulation captures the nonlinear (large) deflection behavior of the wings, the effects of anisotropic piezoelectric composites embedded in the skin, and the unsteady subsonic aerodynamic forces acting on the wing. Because the wing is long and slender, it can be modeled as a beam undergoing three dimensional displacements and rotations. The cross sectional stiffness, inertia, and actuation properties of the wing are calculated along the span, and then incorporated into the 1-D nonlinear beam model derived in this paper. Finite-state unsteady subsonic airloads are incorporated to complete the state space aeroelastic model. Some of the capabilities of the formulation are exemplified within the numerical studies. Two baseline vehicles are designed: one with APA incorporated in the outer wing so to generate wing warping, and the second based on a 50%-span aileron. Different results include static and dynamic instabilities associated with the joined-wing configuration, roll rate and roll angle performance, and the overall ability of the different concept to produce maneuver loads. Finally, discussion on required material technology improvements to make the wing-warping authority par with the aileron for a joined-wing configuration is presented.

---

* Associate Professor of Aerospace Engineering. Associate Fellow, AIAA. Member, AHS.
† Graduate Research Assistant. Mechanical Engineering. Currently Research Engineer, C.S. Draper Labs., Cambridge, Massachusetts.

Introduction

The first successful heavier-than-air flight took place 100 years ago. The Wright Flier used the motion of the pilot's hips to control the warping of the wing and, therefore, the vehicle roll. The relatively soft-in-torsion wings were replaced by stiffer designs with the increase on vehicle flying speeds. The lack of authority to twist the stiffer wings resulted in replacing wing warping with discrete aileron control. Within this concept, maneuver loads are generated at discrete movable parts of the wings in contrast to the reshaping of the wing.

Two decades ago, the concept of active aeroelastic wing (AAW) was introduced. There, instead of generating maneuver loads from a set of control surfaces and fight the flexibility of the wing, the control surfaces are used to induce deformation on the wing so that the reshape of the wing is responsible for generating such loads. Different numerical studies have been pursued, showing promises of achieving different objectives while reducing overall systems weight[1]. A modified F/A-18A with a relatively flexible wing was constructed as a testbed for this concept and just recently has started flight tests at NASA Dryden.

More recently, with the advancement of active materials and the development of anisotropic piezo-composite actuators (APA)[2,3], one may be able to once again implement wing warping for maneuver load generation. Through APA embedded as an integral load-bearing component of the wing structure, local strains can be induced at certain areas of the wing structure and in certain directions. Those strains are controlled externally by applied electric field to the actuators. By properly designing the active structure, a single physical structural realization can achieve several different aeroservoelastic objectives, presenting itself as a truly active aeroelastic tailoring mechanism. Moreover, this could bring the AAW concept to its fulfillment, and represents a fundamental step towards the development of a more generic morphing aircraft.

Among the types of aircraft that could take advantage of such concept, high-altitude long-endurance ones are the most likely candidates. Due to mission requirements, those vehicles present high-aspect-ratio wings that result in relatively flexible structures. If the conventional design paradigm is to be used, the wing flexibility has to be counteracted by additional structural reinforcements that will result in extra mass penalty. Some basic studies exploring APA for active aeroelastic tailoring of such vehicles[4] show that multiple objectives can be achieved by the same wing realization. Studies were conducted for flutter boundary enhancement and gust load response. It is worthwhile mentioning here that the wing's high flexibility result in nonlinear structural motions. This adds another degree of complexity to this already reach domain in which the structural dynamics of the flexible vehicle must be modeled accordingly.

A recent work[5] by the authors investigates in-depth the effects of using APA in three classes of Uninhabited Aerial Vehicles (UAV): small (e.g., Pointer), medium (e.g., Predator), and large (e.g., Global Hawk). For that study, a framework was created for analyzing and designing different high-aspect-ratio wing vehicles. A new strain-based active structural formulation was created and implemented in the framework. The three classes of UAVs were studied for both wing warping and aileron controls. Different objectives included: roll controllability, flutter enhancement, and gust load alleviation and response. Also, an assessment of the structural weight penalty incurred for using current technology APA was conducted. Although the final decision has to be made at the system's level (including mission effectiveness, survivability, etc.) and a formal numerical optimization study is still needed, results from Ref. 5 show that wing warping is possible today by employing APA as part of the composite wing construction. Basic performance results of the active wing are comparable with the ones from a wing with ailerons.

The intent of the present paper is to perform similar investigations as in Ref. 5 on a joined-wing Sensorcraft configuration. This is a new high-altitude long-endurance ISR platform that carries a variety of sensors.

Due to the unusual shapes of joined-wing airplane configurations, the effects of structural deformation on the static aerodynamic and aeroelastic behavior are difficult to intuit and predict. Deformation of the structure at a certain location may produce large changes in angle of attack in the lifting surfaces at other locations. Efforts to minimize structural weight may create aeroelastic instabilities that are not encountered in conventional aircraft design. For joined-wing aircraft, the first sign of failure may be in the buckling of the aft members as the structure is softened. Flutter and divergence may also become a problem in these members due to the reduction in structural frequency as they go into compression. As the aircraft becomes more flexible, the nature of the geometric structural nonlinearities become more important and the lift distribution on the aircraft may be adversely affected.

Livne[6] presented a thought provoking survey on the design challenges of joined-wing aircraft configurations. Therein, he presents a review of past works in joined-wing aeroelasticity and gives a qualitative discussion of their behavior in a multidisciplinary context. Much of the discussion in the paper deals with structural and aeroelastic issues relating to the aft wing/tail. The in-plane loads due to structure deformation and changes in geometric stiffness give rise to non-intuitive aeroelastic behavior. Bending and twisting couplings of the entire structure cause natural frequencies and mode shapes to shift. The tendency for buckling and divergence in the aft member is of major concern when trying to reduce weight. The finding of rear wing divergence to be more critical than flutter is counterintuitive, since the aft wing is supported at the joint. This phenomenon seems associated with a reduction in structural stiffness due to the in-plane compressive loads in the rear members. The geometry of the joint between forward and aft wings is also of importance because it influences how in-plane, bending, and torsion loads are transferred. For instance, a pinned joint may allow upward buckling of the aft wing, while a fixed rigid joint may allow the aft wing to buckle downward, since bending moments are transferred across the joint.

While no firm design of a joined-wing Sensorcraft exists in public literature, Refs. 7 and 8 present a systematic design optimization study for the basic vehicle with regular control mechanisms. The authors proposed an integrated design method that brings together different software packages like NASTRAN and PanAir, and integrate then through the Air Vehicles Technology Integration Environment (AVTIE). Their most recent work[8] addresses some of the nonlinear structural issues present in the joined-wing configuration and discuss the impact of different constraints on a fully stressed design. Ref. 9 employs multiple control surfaces on the different wing segments to implement the AAW concept on the joined-wing Sensorcraft. There, the authors employ a linear aeroelastic representation of the lifting surfaces to optimize trim so that to minimize the overall structural deformation (that may affect antenna performance). It was numerically shown that the vehicle could be trimmed for 1-g flight using six

American Institute of Aeronautics and Astronautics

independent control surfaces and simultaneously minimizing structural deformation.

Active distributed control using embedded piezocomposites in the wing structure may be able to improve the performance in several ways, and also may allow for lighter designs by actively offsetting critical instabilities. Warping the structure in order to change the aerodynamic force distribution across the vehicle may be a means of eliminating or reducing unwanted structural couplings due to deformation. The degrading effects of in-plane loads on the aft members may be dealt with through the use of active/passive internal structural couplings. Passive structure design may be incapable of dealing with the global structural load transfers at all flight conditions. By embedding active materials in large areas of the vehicle, the global behavior of the structure may be enhanced. Actuators embedded in the forward wings will be able to respond to stresses measured in the aft wings. Actuators anywhere in the structure can respond to measurements taken everywhere over the structure. This may allow for global modal behavior to be adjusted by timing and shaping the internal stresses in the structure.

The state of the art in passive composite structure design exploits structural couplings to prevent aeroelastic instabilities. While this may work for certain instabilities at certain flight conditions, it may have a negative effect on other aeroelastic characteristics at other flight conditions. The ability to actively adjust the structural couplings would have obvious benefits. Before any claims can be made, however, it is necessary to determine the scale of the problem and the relative amount of active material to passive material required to accomplish this goal.

The potential for new ideas in this area seems limitless. For now, however, this paper concentrates in two key issues:
1. New proposed formulation for highly flexible active vehicle analyses and the importance of geometrically nonlinear structural modeling;
2. Assessment of wing warping as a means of roll control of a joined-wing configuration based on state-of-the-art anisotropic piezocomposite actuator technology.

Formulation

For the present study, the vehicle is allowed six rigid body degrees of freedom as well as flexible degrees of freedom. The wings are allowed fully coupled three-dimensional bending, twisting, and extensional deformation. Flaps and ailerons may be included for comparison purposes and for the study of hybrid vehicle control. A finite-state unsteady airloads model based on the work of Peters[2] is integrated into the system equations. The model allows for a low order set of nonlinear equations that can be put into state-space form to facilitate control design.

Element Description: Specialized nonlinear beam elements were created for the ongoing work, each having four strain degrees of freedom, representing extension, twist, and two bending strains. Deformations of this element are exemplified in Fig. 1. With a constant strain distribution over the element, a wide range of geometrically nonlinear shapes can be obtained. A single element, for example, can be deformed into a circle or spiral shape.
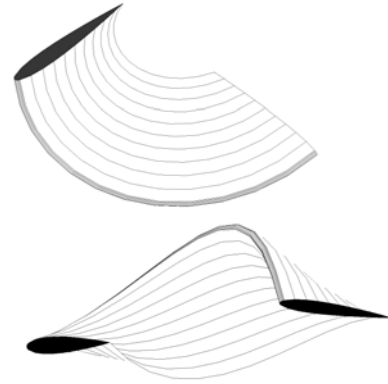

Figure 1: Deformations represented by a single element with constant strain distribution

The kinematics of the element are described as follows. The beam reference frame is denoted w, and is a function of the beam coordinate, s. The position and orientation of a point on the reference line can be described by the 12x1 vector h as

$$h(s) = [p_w(s)^T, w_x(s)^T, w_y(s)^T, w_z(s)^T]^T \qquad (1)$$

where p_w is the position of frame w in the body coordinate system and w_x, w_y, and w_z are the direction vectors pointing along the beam axis, toward the leading edge, and normal to the airfoil, respectively, defined in the body frame. The partial differential equation governing how h moves through space involves the strain variables,

$$\frac{\partial h(s)}{\partial s} = A(s)h(s) \qquad (2)$$

with

$$A(s) = \begin{bmatrix} 0 & 1+\varepsilon_x(s) & 0 & 0 \\ 0 & 0 & \kappa_z(s) & -\kappa_y(s) \\ 0 & -\kappa_z(s) & 0 & \kappa_x(s) \\ 0 & \kappa_y(s) & -\kappa_x(s) & 0 \end{bmatrix}$$ (3)

where the blocks are all 3x3 diagonal matrices. When the element is assumed to have a constant strain vector, the solution can be obtained

$$h(s) = e^{As}h_0 = e^{G(s)}h_0$$ (4)

where h_0 is the is the element boundary condition. The total virtual work done on an element due to all internal and external forces and moments can be written as

$$\delta W = -\delta h^T M\ddot{h} - \delta\varepsilon^T K\varepsilon + \delta\varepsilon^T B_v v +$$
$$- \delta h^T Ng + \delta p^T B_F F^{dst} + \delta\theta^T B_M M^{dst} +$$ (5)
$$+ \delta p^T F^{pt} + \delta\theta^T B_M M^{pt}$$

where the terms involved include the effects of inertial, gravitational, internal strain, piezoelectric, distributed, and point forces and moments.

Member Equations: Each member is an assemblage of elements and may include breaks in the beam reference line at the joint between elements and variation in the level of discretization.
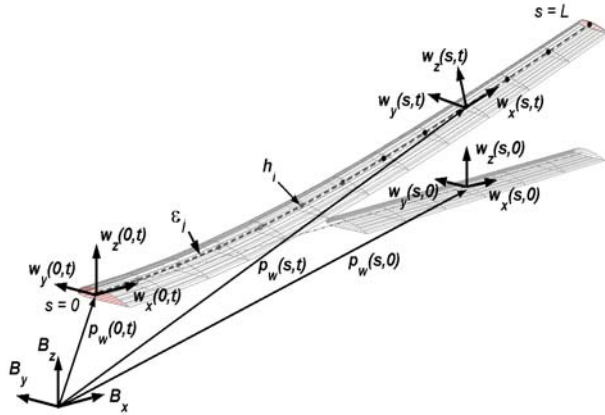
Figure 2: Illustration of a single undeformed and deformed member with different refence frames.

The kinematics for a member is obtained by marching the element kinematics from the boundary node to the end of the last element, using the values of the strain variables in each element to march forward. This procedure is given for the three node elements used in the present model,

	Element 1	Element 2	...	Element n
Node 1	$h_{11} = h^*$	$h_{21} = D_{21}h_{13}$	...	$h_{n1} = D_{n,n-1}h_{n-1,3}$
Node 2	$h_{12} = e^{G_1}h_{11}$	$h_{22} = e^{G_2}h_{21}$	...	$h_{n2} = e^{G_n}h_{n1}$
Node 3	$h_{13} = e^{G_1}h_{12}$	$h_{23} = e^{G_2}h_{22}$	...	$h_{n3} = e^{G_n}h_{n2}$

(6)

where h_{ij} is the jth node of the ith element and the D_{ij} matrices contain elements of the direction cosines, accounting for the break at the element junction. Eq. (6) can be put into matrix form

$$\bar{A}h = h^*$$ (7)

where h is now a column matrix containing nodal position and orientation variables for all of the nodes in the member, and h^* is a column matrix containing the boundary condition. When the member is fixed at the first node and the element has three nodes, this relation is given by

$$\begin{bmatrix} I & 0 & 0 & 0 & 0 & 0 & 0 \\ -e^{G_1} & I & 0 & 0 & 0 & 0 & 0 \\ 0 & -e^{G_1} & I & 0 & 0 & 0 & 0 \\ 0 & 0 & D_{21} & I & 0 & 0 & 0 \\ 0 & 0 & 0 & -e^{G_2} & I & 0 & 0 \\ 0 & 0 & 0 & 0 & -e^{G_2} & I & 0 \\ 0 & 0 & 0 & 0 & 0 & D_{32} & \ddots \end{bmatrix} \begin{bmatrix} h_{11} \\ h_{12} \\ h_{13} \\ h_{21} \\ h_{22} \\ h_{23} \\ \vdots \end{bmatrix} = \begin{bmatrix} h^* \\ 0 \\ 0 \\ 0 \\ 0 \\ 0 \\ \vdots \end{bmatrix}$$ (8)

The D_{ij} matrices are equal to the identity matrix if the elements are aligned, and contain rotation variables if the beam reference line makes a break at an element intersection.

The Jacobian matrix relating changes in the element strain variables to changes in the position and direction vectors, taken about the current strain vector ε_0, is given by

$$dh = [\tfrac{\partial h}{\partial \varepsilon}]d\varepsilon = J_{h\varepsilon}d\varepsilon$$ (9)

where

$$J_{h\varepsilon} = -\bar{A}_0^{-1}\left[\tfrac{d}{d\varepsilon}\left(\bar{A}(\varepsilon)h_0\right)\right]$$ (10)

is found though an iterative routine. The total virtual work done on a member due to all internal and external loads has the same form as Eq. (5), except that the size has increased by a factor of n, where n is the number of elements in the member.

Global Finite Element Matrices: At this point, each wing member represents an independent entity, for

4
American Institute of Aeronautics and Astronautics

which equations of motion may be constructed. However, because inter-member constraints will be imposed, it is more convenient to assemble the individual member matrices into a global equation for the virtual work. Before applying the inter-member constraints, the expression for work takes on the same form, where the matrices are in an uncoupled block diagonal form, and can be written as

$$\delta W = -\delta h^T (M\ddot{h} - \delta h^T Ng) - \delta \varepsilon^T (K\varepsilon - B_v v) + \\ + \delta p^T (B_F F^{dst} + F^{pt}) + \delta \theta^T (B_M M^{dst} + M^{pt}) \qquad (11)$$

Inter-member constraints are used to enforce that a node position, which is coincident to two members, remains coincident and that the relative orientation of the member coordinate systems at those nodes remains fixed. Let two members be initialized such that in their undeformed state they share a common node location. Each node has three coordinate frames associated with it. Frame w is the beam frame and is aligned with the beam axes as described above. Frame b is aligned with the body frame, B, when the member is undeformed. Frame a is aligned with the airfoil local coordinate system. In the case of a wing with zero root angle of attack and zero sweep and dihedral, frames w, b, and a are in alignment, but in general this is not the case.

The nodal position and orientation vector, h, can be defined for three corresponding frames, e.g.,

$$h^w = [p_w^T, w_x^T, w_y^T, w_z^T]^T \\ h^b = [p_b^T, b_x^T, b_y^T, b_z^T]^T \\ h^a = [p_a^T, a_x^T, a_y^T, a_z^T]^T \qquad (12)$$

where the following constant relations hold

$$h^b = D^{bw} h^w, \quad h^a = D^{aw} h^w$$

$$D^{bw} = \begin{bmatrix} 1 & 0 & 0 & 0 \\ 0 & C_{11}^{wb} & C_{21}^{wb} & C_{31}^{wb} \\ 0 & C_{12}^{wb} & C_{22}^{wb} & C_{32}^{wb} \\ 0 & C_{13}^{wb} & C_{23}^{wb} & C_{33}^{wb} \end{bmatrix} \qquad (13)$$

$$D^{aw} = \begin{bmatrix} 1 & 0 & 0 & 0 \\ 0 & C_{11}^{wa} & C_{21}^{wa} & C_{31}^{wa} \\ 0 & C_{12}^{wa} & C_{22}^{wa} & C_{32}^{wa} \\ 0 & C_{13}^{wa} & C_{23}^{wa} & C_{33}^{wa} \end{bmatrix}$$

The D matrices here are 12x12 matrices where each block is a 3x3 diagonal matrix and C^{wb} and C^{wa} are components of the rotation matrices from frames b and a, respectively, to frame w. It should be clear now that the vector h is simply a way to express the position and

orientation of a coordinate system in a single vector format, and that the D matrices are a rearrangement of the standard direction cosines matrices.

If node m of member i is initially coincident with node n of member j, then coordinate systems b_m^i and b_n^j are equivalent for the undeformed geometry. To enforce the inter-member constraint, it is required that

$$h_{i,m}^b = h_{j,n}^b \rightarrow D_{i,m}^{bw} h_{i,m}^w = D_{j,n}^{bw} h_{j,n}^w \qquad (14)$$

This can be done by associating a large virtual work penalty term if the equality in Eq. (14) is violated, that is,

$$\delta W = \\ -(D_{i,m}^{bw} \delta h_{i,m}^w - D_{j,n}^{bw} \delta h_{j,,n}^w)^T \hat{K} (D_{i,mi}^{bw} h_{i,m}^w - D_{j,n}^{bw} h_{j,n}^w) \qquad (15)$$

which can be rearranged into the matrix form

$$\delta W = -[\delta h_{i,m}^T, \delta h_{j,n}^T] \begin{bmatrix} D_{i,m}^{wb} \hat{K} D_{i,m}^{bw} & -D_{i,m}^{wb} \hat{K} D_{j,n}^{bw} \\ -D_{j,n}^{wb} \hat{K} D_{i,m}^{bw} & D_{j,n}^{wb} \hat{K} D_{j,n}^{bw} \end{bmatrix} \begin{bmatrix} h_{i,m} \\ h_{j,n} \end{bmatrix} \\ = -[\delta h_{i,m}^T, \delta h_{j,n}^T] \begin{bmatrix} K_{11} & K_{12} \\ K_{21} & K_{22} \end{bmatrix} \begin{bmatrix} h_{i,m} \\ h_{j,n} \end{bmatrix} \qquad (16)$$

To impose the inter-member constraint, Eq. (11) is augmented with a stiffness matrix acting on the nodal position vector, becoming

$$\delta W = -\delta h^T (M\ddot{h} + C_C \dot{h} + K_C h - \delta h^T Ng) - \delta \varepsilon^T (K\varepsilon - B_v v) \\ + \delta p^T (B_F F^{dst} + F^{pt}) + \delta \theta^T (B_M M^{dst} + M^{pt}) \qquad (17)$$

where K_c is a matrix of zeros except in the rows and columns corresponding to the entries in Eq. (16). For numerical stability, a constraint damping matrix C_c is also added to Eq. (17) in the same way. Some care is required in selecting the constraint damping and stiffness constants.
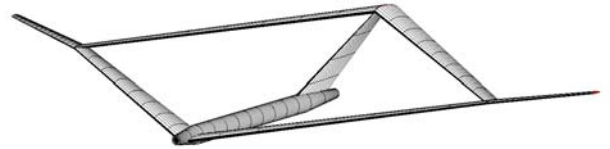

Figure 3: Illustration of a built up joined-wing structure with inter-member constraints imposed

Equations of Motion: With the six rigid body degrees of freedom, the system structural degrees of freedom are represented by the column matrix q, where

$$\dot{q} = [\dot{\varepsilon}_1^T, \dot{\varepsilon}_2^T, \ldots, \dot{\varepsilon}_n^T, V_B^T, \omega_B^T]^T \qquad (18)$$

and ε_i contains the strain variables for wing member i, V_B and ω_B are the linear velocity and angular velocity of the vehicle, respectively, represented in the body frame, B. The dependent variables for the entire vehicle are put into the column matrix H,

$$\dot{H} = [\dot{h}_1^T, \dot{h}_2^T, \ldots, \dot{h}_n^T, V_B^T, \omega_B^T]^T \qquad (19)$$

The dependent degrees of freedom are related to the independent degrees of freedom through a Jacobian matrix relation

$$H = f(q), \quad dH = [\tfrac{\partial H}{\partial q}]dq = [J_H(q)]dq \qquad (20)$$

The expression for virtual work on the vehicle is now given by

$$\begin{aligned} \delta W = \delta q^T (&-\bar{M}\ddot{q} - \bar{C}\dot{q} - \bar{K}q + \bar{N}g + \bar{B}_v V + \bar{B}_{F1}F^{dst} + \\ &+ \bar{B}_{F2}F^{pt} + \bar{B}_{M1}M^{dst} + \bar{B}_{M2}M^{pt} + \\ &+ B_{q0}q_0 + B_H H) \end{aligned} \qquad (21)$$

The principle of virtual work requires that the total virtual work done on the system be equal to zero, leading to the equations of motion,

$$\begin{aligned} \bar{M}\ddot{q} + \bar{C}\dot{q} + \bar{K}q = \\ B_V V + B_{F1}F^{dst} + B_{F2}F^{pt} + B_{M1}M^{dst} + \\ + B_{M2}M^{pt} + \bar{N}g + B_{q0}q_0 + B_H H \end{aligned} \qquad (22)$$

The distributed loads are divided into aerodynamic loads and user supplied loads. The aerodynamic loads evaluated at the current state have the incremental form

$$\begin{aligned} F^{aero}(t) = F^{aero}(t_0 + \Delta t) \\ \approx F_0(q_0, \dot{q}_0, \lambda_0) + F_{\ddot{q}}\ddot{q} + F_{\dot{q}}\Delta\dot{q} + F_q\Delta q + F_\lambda\Delta\lambda \end{aligned}$$
$$(23)$$
$$\begin{aligned} M^{aero}(t) = M^{aero}(t_0 + \Delta t) \\ \approx M_0(q_0, \dot{q}_0, \lambda_0) + M_{\ddot{q}}\ddot{q} + M_{\dot{q}}\Delta\dot{q} + M_q\Delta q + M_\lambda\Delta\lambda \end{aligned}$$

where λ is column matrix of induced flow states as described in Ref. [10]. The induced flow states are governed by a differential equation of the form

$$\dot{\lambda} = L_1\lambda + L_2\ddot{q} + L_3\dot{q} \qquad (24)$$

The aeroelastic equations of motion are obtained by moving the state dependent aerodynamic loads over to the left hand side of Eq. (22) and augmenting the structure states with the induced flow states, which can be represented in state space form as

$$\dot{x} = A(x)x + B(x)u(x,t) \qquad (25)$$

where the state vector is now given by

$$x = [\dot{q}^T, q^T, \lambda^T]^T \qquad (26)$$

Numerical Results

For the numerical study, baseline vehicles are created for the wing warping (active) and for the aileron (passive) concepts. For both cases, controllable changes in aerodynamic loads only occur in the outer wing. The active wing contains APAs that can produce 1350 µstrain of free strain amplitude and are distributed along the entire span. The passive wing contains a 50%-span/20%-chord aileron that is allowed 30° of amplitude deflection.

Once the baselines are designed, different sensitivity studies are presented to exemplify further capabilities of the proposed framework and the relative performance of wing-warping controlled configuration with respect to an aileron-controlled one

Baseline Vehicles
Two distinct designs are needed to study the effects of wing warping and its relative performance with respect to an aileron-controlled vehicle. First, a design that represents an active wing with embedded APA. Second, a passive wing designed to have an aileron. Three sets of constraints were defined to help guide the baseline designs: laminate strength (based on first-ply failure) at 2.5-g load, laminate strength based on gust loads, and minimum linearized flutter margin. For all the cases, the fuselage and tail are assumed rigid (Fig. 4).

Vehicle Model Description: From top view, the vehicle shape is symmetric (although one may want to vary the forward/aft location of the joint). The wings are denoted right forward inboard, left forward inboard, right rear inboard, left rear inboard, right outboard, and left outboard. Right and left are determined as in Fig. 5 (as viewed from top with nose pointing up). Dimensions are given in Table 1. Each of the six wing members is divided into four regions for definition of cross-section layup and ply thickness distribution. The forward and rear members are identical in construction, and the material distribution will follow the numbering convention as indicated in Fig. 5.
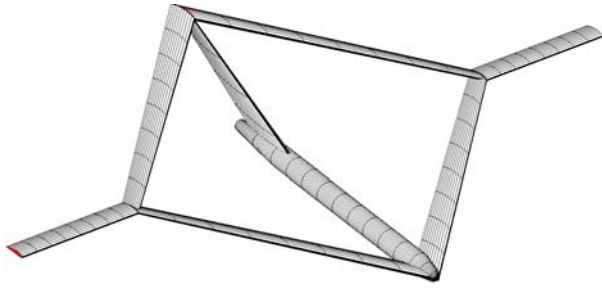
Figure 4: Baseline joined-wing Sensorcraft vehicle with unswept outer wings (where APA actuators or ailerons are present).
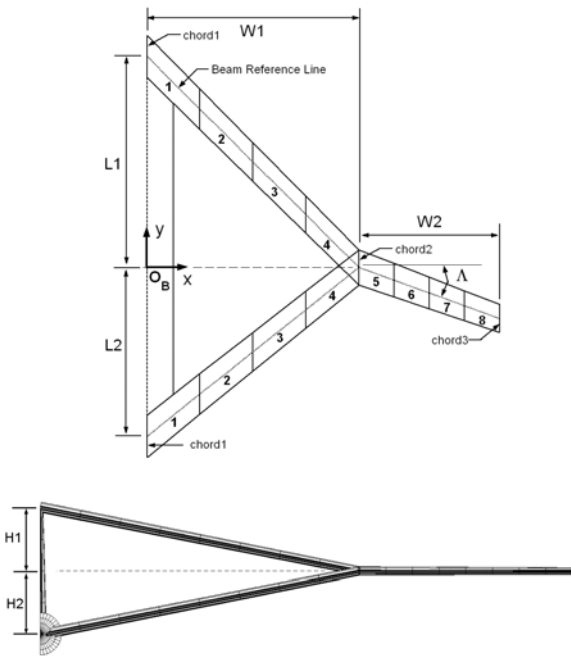

Figure 5: Baseline joined-wing Sensorcraft vehicle geometry.

Mission Profile: Seven flight index points represent the nominal mission profile, as indicated in Fig. 6. At each index point, the altitude, fuel mass, and nominal flight velocity are specified. The index points represent: (1) takeoff, (2) climb, (3) cruise ingress, (4) cruise/loiter/cruise, (5) cruise egress, (6) decent, and (7) landing. The fuel burn determines the duration of each flight segment. The nominal flight speed at each index point is based on the cruise speed (input parameter), and is computed such that the dynamic pressure is constant (constant indicated air speed). The trim body angle is also obtained at each index point for a set of equally spaced increasing flight speeds, up to 200% of the nominal speed at that flight index.

Table 1: Baseline joined-wing Sensorcraft vehicle planform data.

L1 = L2	15 m
W1 = W2	20 m
H1 = H2	4 m
chord1	3.5 m
chord2	2 m
chord3	1.5 m
Sweep angle (Λ)	0°
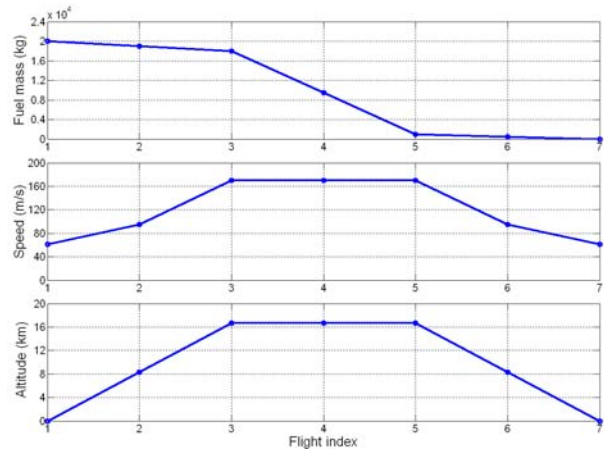
Figure 6: Nominal mission profile.
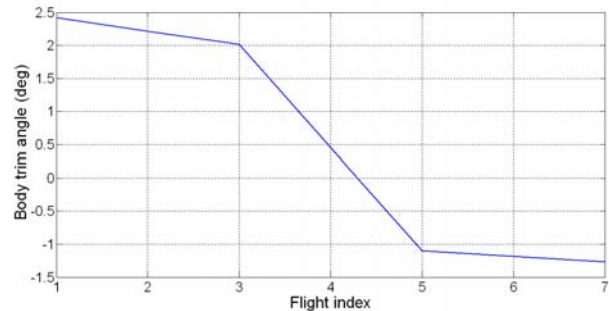
Figure 7: Active vehicle body trim angle as a function of flight index (nominal fight speed at each index point)—similarly for aileron concept.

Vehicle Trim: At each flight index point, the vehicle is trimmed for equilibrium in horizontal flight at a given flight speed. The trim angle is shown in Fig. 7 for the nominal flight speeds.

Vehicle Mass Breakdown: The vehicle mass breakdown is given in Table 2. The fuel is assumed to be distributed evenly throughout the inner and outer wings, independent of the total amount of fuel on board. The fuselage contains no fuel.

Table 2: Vehicle Mass Distribution.

Cruise altitude	16,700 m
Cruise speed	170 m/s
Fuselage structure + payload + engine mass	4,000 kg
Fuel mass	20,000 kg
Active vehicle total wing structure mass	11,191 kg
Passive vehicle total wing structure mass	10,459 kg
Added mass for aileron mounts/wing	58.9 kg

Wing Cross Section: For simplicity, NACA 4415 was chosen as the airfoil and it is kept constant throughout the wing members (see Fig. 8). A single spar is used at 45% chord. (This could be easily replaced with a two-spar configuration, particularly for the inner wings. This, however, reduces the computational time for each design iteration and does not qualitatively affect the results.) The wing reference axis is indicated in Fig. 8. For the final wing layup, the top and bottom skins have ply groups composed of [0/45/-45/0] and the web with ply groups of [0_4]. For the active outer wing, the "45" and "–45" ply groups are APA. Everything else is S-glass. Material properties are given in Table 3. The thickness distribution for each element within a wing member (according to the numbering scheme defined in Fig. 5) is given in Figs. 9 and 10 for the active and passive wings, respectively. The web thickness is four times the thickness of a 0° ply group at a given span member. The maximum induced twist angle distribution along the span generated by the APA is shown in Fig. 11.

Table 3: Material properties (1—fiber direction; 2—transverse to fiber; 6—shear)

	S-glass/epoxy	APA
Mass (kg/m^3)	1855	4100
Q_{11} (GPa)	48.0	34
Q_{12} (GPa)	3.5	7.5
Q_{22} (GPa)	12.2	17
Q_{66} (GPa)	3.6	5.1
Max. free strain (με)	N/A	2700
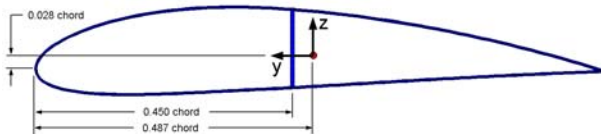
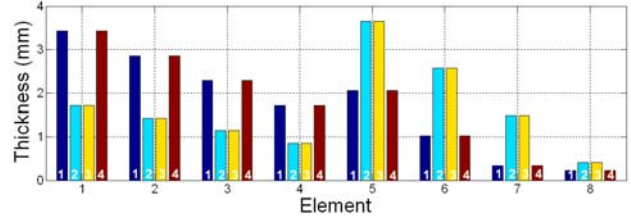Figure 8: NACA 4415 cross-section geometry.

Figure 9: Ply group thickness for each element (see Fig. 5), active wing. The bar numbers indicate the ply number in the wing skin.
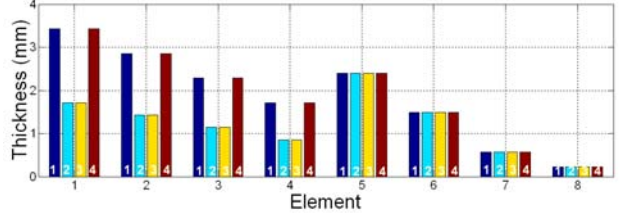

Figure 10: Ply group thickness for each element (see Fig. 5), passive wing. The bar numbers indicate the ply number in the wing skin.
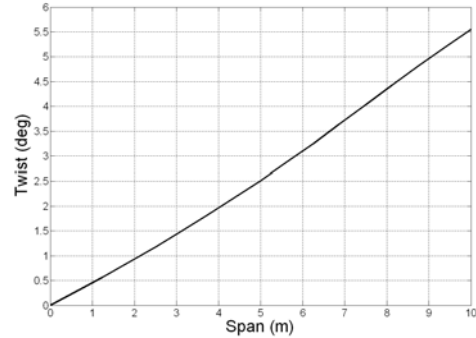

Figure 11: Twist distribution along the outer wing due to 1350 μstrain actuation.

Design Constraint 1 (2.5 g load condition): To evaluate DC1, the vehicle is flown in level flight at sea level. The speed is increased until the lift equals 2.5 times the weight. The vehicle is fully fueled to represent the worst-case scenario. Fig. 12 shows the vehicle deformation and distribution of aerodynamic forces under these conditions. The wing vertical bending displacements are plotted in Figs. 13 and 14 for the active and passive configurations, respectively. The deflection at the wing tip is approximately 12% of the semi-span. Similarly, the (absolute value of the) maximum ply strains are plotted in Figs. 15 and 16. The strains are with respect to the fiber direction (11-along fiber, 22-transverse to fiber, 12-shear). The constraint imposed here is that the maximum strain does not surpass 3,000 microstrain in any of the components. The ply thicknesses in each wing region were minimized until the design strain limits were

approached. DC1 is now considered the active constraint, and will remain so unless DC2 (gust load structure failure) or DC3 (flutter failure) becomes active.
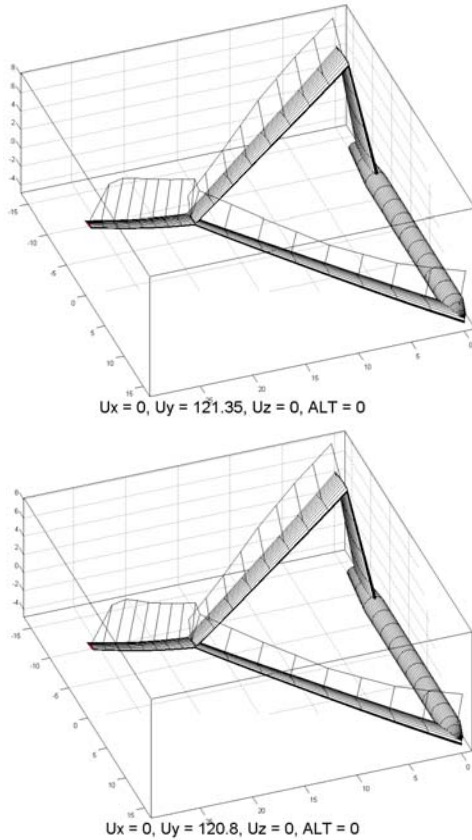

Figure 12: Active (top) and passive (bottom) vehicles at 2.5 g loading condition (note lift loss at the wing tip).

Figure 13: Wing deflections for active vehicle (lift/weight = 2.5, sea level, fully fueled, U = 121.3m/s).

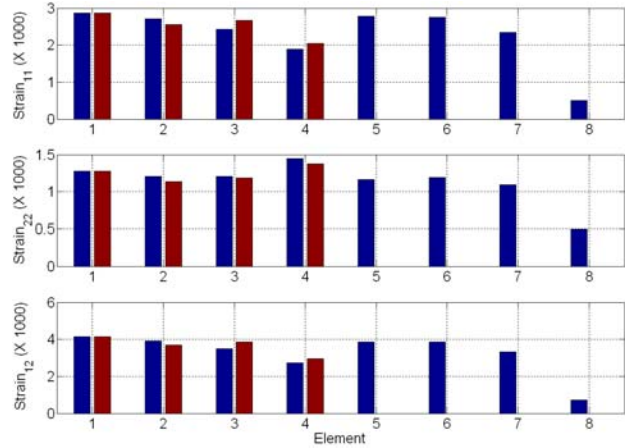Figure 14: Wing deflections for passive vehicle (lift/weight = 2.5, sea level, fully fueled, U = 120.8m/s).

Figure 15: Maximum ply strains in each element during 2.5 g loading condition, active vehicle.
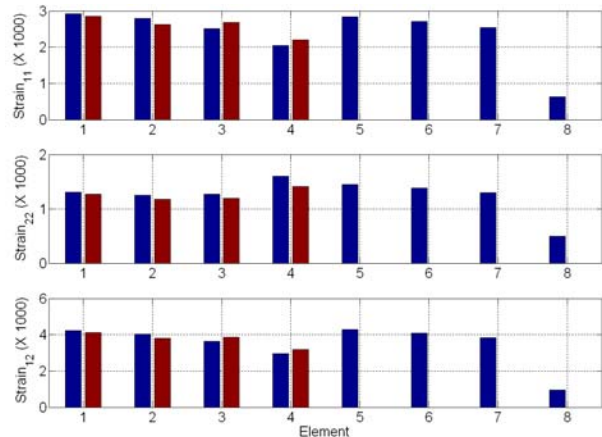
Figure 16: Maximum ply strains in each element during 2.5 g loading condition, passive vehicle.

Design Constraint 2 (gust load failure): The worst-case gust loading occurs when the wings are depleted of fuel (no inertia relief) and the vehicle is traveling at sea-level and nominal speed. The slowest flight speed maximizes the vertical gust-induced angle of attack ($\alpha_{gust} = \tan^{-1}(w/U)$). Even though the framework implements the Dryden gust model, for this design exercise, the "1-cosine" gust model is used for simplicity. The amplitude of the 1-cosine vertical gust is 10 m/s (22.4 mph). The response is shown in Fig. 17. The maximum ply strains as function of time are shown in Fig. 18. As one can see, the maximum values are still well below the imposed limit on the maximum ply strains.

Design Constraint 3 (flutter speed): The flutter speed is approximated at each flight index point by determining the stability characteristics of the linearized system about its nonlinear equilibrium condition. The minimum linearized flutter margin along the mission profile is imposed to be 25% above the corresponding

9
American Institute of Aeronautics and Astronautics

nominal flight speed. As it can be seen from Table 4, both designs satisfy that limit without much difficulty. This could be relaxed in the future by allowing actively enhancement of the flutter boundary.
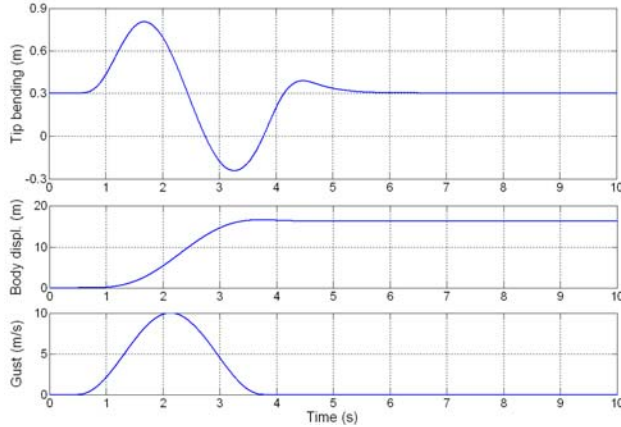

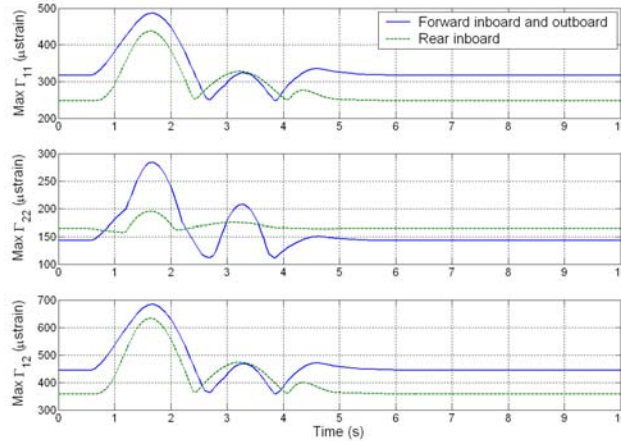Figure 17: Response to gust input, sea-level, flight index 7, active wings (similar for passive wings).

Figure 18: Maximum ply strains (absolute value) during gust encounter, active wings (similar for passive wings).

Table 3: Flutter speed margins for the active and passive (aileron) vehicles at each flight index.

Flight index	Nominal speed m/s	Margin/ Active %	Margin/ Aileron %
1	61.21	33.97	36.45
2	95.30	32.23	33.78
3	170.0	34.09	34.31
4	170.0	34.53	35.13
5	170.0	28.89	26.34
6	95.30	34.29	39.67
7	61.21	46.45	66.74

Characteristics of the Two Vehicle Concepts

Once the baselines have been established, different studies on the vehicles can be conducted. The ones chosen to be presented here illustrate some of the capabilities of the formulation, the unique behavior of joined-wing configurations, and the relative performance of wing warping and aileron control schemes for vehicle primary roll control.

Effects of Load Factor on the Stability of the Rear Wing: Since the aft wings are primarily under compression, their buckling response can be a sizing limitation for the vehicle. For the particular baseline designs considered here, deformation of the rear inboard wing increases dramatically when the load factor reaches about 2.7, bring the whole wing system close to a collapse (see Fig. 19). This condition is naturally modeled in the presented framework through the nonlinear structural analysis.
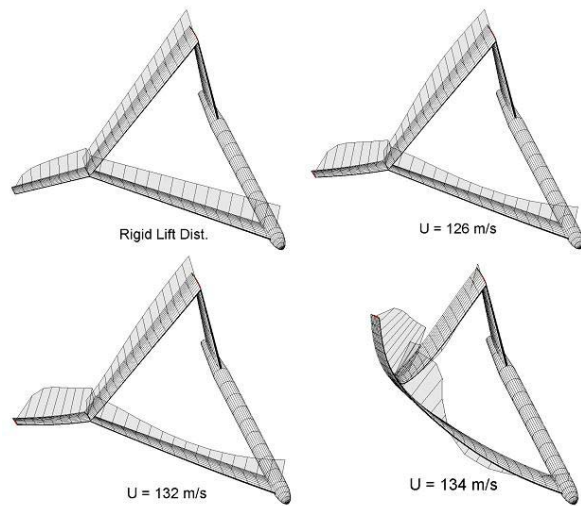

Figure 19: Lift distribution on the vehicle as the buckling speed is approached (sea level, fully fueled, no rigid body degrees of freedom, zero body angle of attack)

To exemplify this, a half-vehicle model is brought to steady state at level flight (at sea level). Then, its flight speed is varied from 70 m/s to 130 m/s, with a resulting load factor ranging from 0.83 to 2.66. The wing shape and deflections are plotted for varying load factor in Figs. 20 thru 24. As may be seen from Figs. 22 and 23, the passive wing configuration is more susceptible to the increase in speed due to a softer outboard wing (higher lift outboard due to aeroelastic effects). The suddenly reduction of the rear wing stiffness results in large bending deflection of the overall wing structure and, consequently, drop in the overall lift (represented by the reduction in load factor as shown in Fig. 24).

This level of wing displacement causes high composite ply strains (stresses), to the point of ply failure. A typical strain component dependence on the load factor is shown in Fig. 25
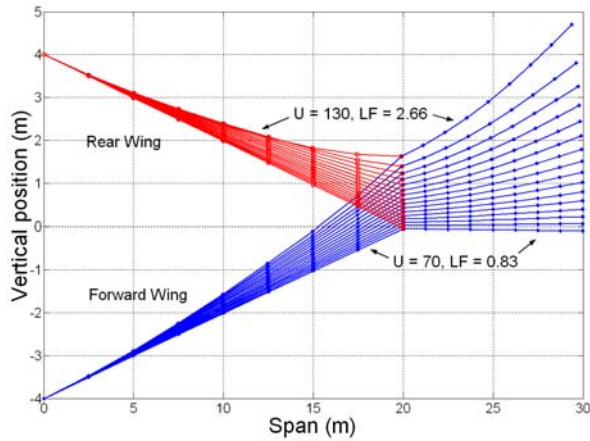

Figure 20: Active wing shape for varying flight speed (level flight at sea level).
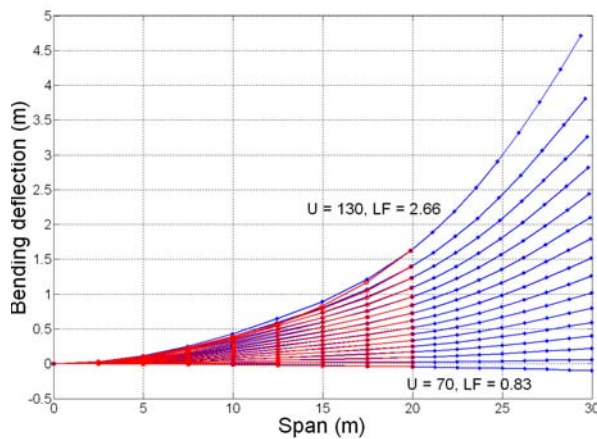

Figure 21: Active wing bending deflections for varying flight speed (level flight at sea level).
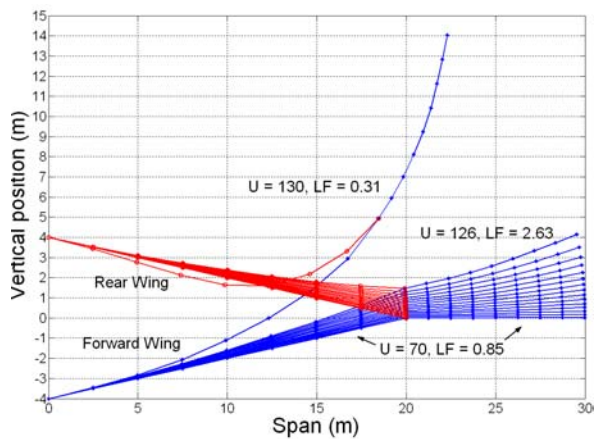

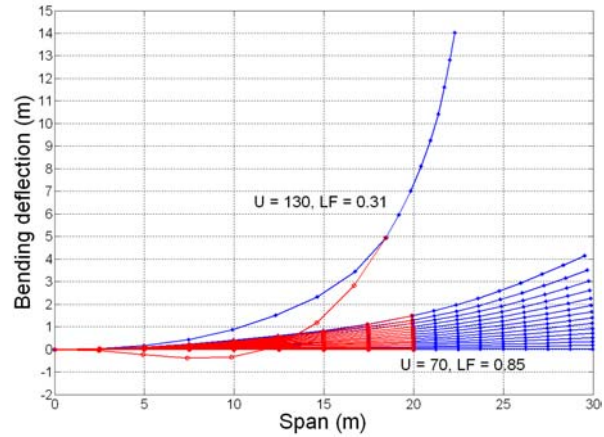Figure 22: Passive wing shape for varying flight speed (level flight at sea level).

Figure 23: Passive wing bending deflections for varying flight speed (level flight at sea level).
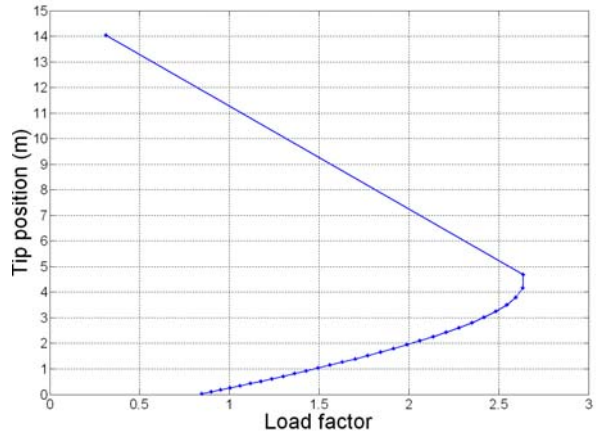

Figure 24: Changes in tip deflection as function of the lift generation capability of the passive wing vehicle at level flight (sea level).
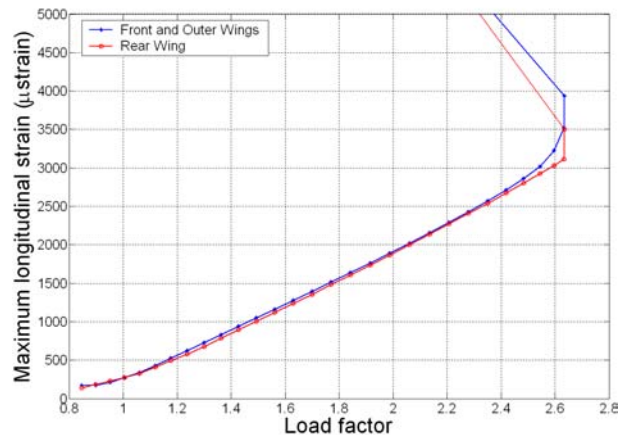

Figure 25: Sample of maximum strain component nonlinear growth due to loss of stiffness on the rear wing with increase load factor (passive wing vehicle at level flight, sea level).
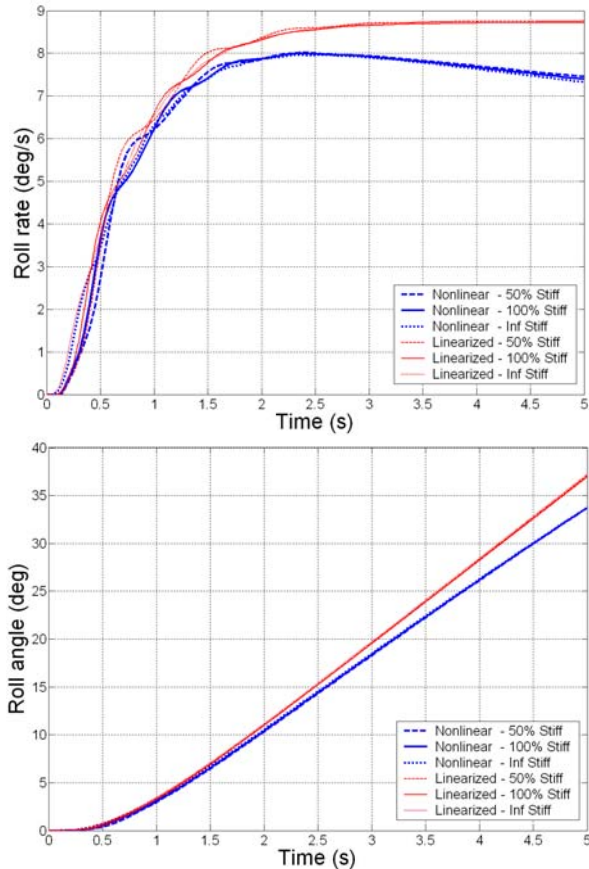
Figure 26: Active concept roll rate and roll angle responses with varying inner wing stiffness (flight index 5, maximum actuation; 100% stiffness is nominal)

Roll Response: To study roll response, two approaches have been implemented: a linearized approach and a nonlinear one. In the linearized approach, the vehicle is first brought to its nonlinear steady state with roll motion locked, and under the influence of applied actuation. Both the static aerodynamic roll moment and roll rate damping moment are computed based on the deformed structure. A representative fuselage roll inertia is used, although the major contributors to roll inertia are the wings. The roll rate response is then solved based on these quantities. This approach has the main advantage of being computationally very efficient. In the nonlinear approach, the vehicle is first brought to its nonlinear steady state with no actuation applied. Then a nonlinear time stepping roll simulation is performed. The input (ply voltage and aileron deflection) is ramped from zero to its maximum value in 0.5 s. Moreover, to assess the impact of the inner wing flexibility to the roll response of the vehicle, two other cases were created: one (denoted as "50% Stiff") where the inner wings have half of the stiffness (extension, bending, and

torsion) of the baseline (denoted as "100% Stiff"), and the other one (denoted by "Inf Stiff") with 100 times the baseline stiffnees, representing an almost rigid case. The roll rate and roll angle responses to applied twist actuation and aileron deflection are shown in Figs. 26 and 27, respectively, for both linear and nonlinear roll calculations during 1-g level flight.
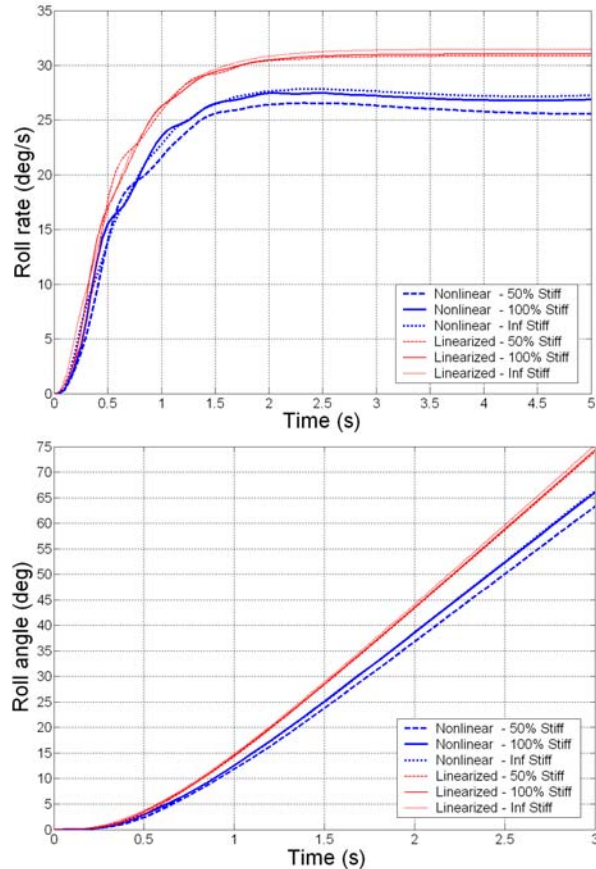

Figure 27: Aileron concept roll rate and roll angle responses with varying inner wing stiffness (flight index 5, maximum deflection; 100% stiffness is nominal)

The very first observation that can be made from Figs. 28 and 29 is that the roll performance level of the wing warping actuation with APA is about three fold lower than the aileron concept. While roll angles of over 50° can be reached by the latter in 2.5 s, for the same time period only 15° is reachable with the active wing. This was expected based on the fact that the quasi-linear twist distribution generated by the active concept reaches 5.5° at the wing tip (where aerodynamic losses are imposed) while the aileron imposes 30° deflection of 25% wing chord between 1/3 and 2/3 of the outer wing span.

For the ways the analysis may be conducted, there is a significant difference between the linearized and fully nonlinear approaches for roll analysis, particularly for the terminal roll rate. In fact, the overshoot that happens due to wing flexibility is not captured at all in the linearized approach. On the other hand, the roll angle response is less sensitivity to the full nonlinear effects, presenting differences between the two analyses predictions of 10% for the active and 15% for the aileron actuations after 3 s into the roll bank.

Regarding the effects on the flexibility of the inner wings, the primary impact is on the dynamics of the response to reach maximum roll rate. For the active concept, due to low roll rates, the effects of the flexibility of the inner wings does not become a factor. However, for the levels of response presented by the ailerons, a significant difference can be seen from Fig. 27. As the inner wings become less stiff, there is a loss on the terminal roll rate due to the deformation of the inner wings. This is only capture by the fully nonlinear analysis.

Outer Wing Sweep Effect on Roll Response: As an indication of the effects of outer wing sweep on roll response, a 25° backward sweep case is compared with the 0° sweep baseline cases. Figs. 28 and 29 show the roll rate results for the active and aileron cases, respectively. Note that the effects of moving the vehicle's aerodynamic center with the outer wing sweep[7] is beyond the scope of this paper even though modeled in the framework. As can be observed from the plots, a decrease in roll rate is observed from both linearized and nonlinear analyses. When the wing is swept, there is a reduction in angle of attack as the wing bends. Since the twist axis of the wing is no longer perpendicular to the airfoil, the effectiveness of twisting the wing to change the angle of attack is decreased. Furthermore, the lift per unit span of the swept wing decreases with the cosine of the sweep angle. Since the roll rate damping of the inner wings is constant as the outer wings are swept, there is an overall reduction in effectiveness of the outer wings to produce roll rate for the same spanwise angle of attack distribution.

APA Technology Impact on Roll Performance: All the studies presented so far were based on representative APA material properties from current existing polycrystalline piezocomposite materials. There have been efforts within the materials research community for the development of different material systems with improved piezoelectric properties. Among them, the single-crystal program[12] for AFC could lead to a significant increase in actuation authority. To estimate the required actuation needed for the joined-wing Sensorcraft-like application, consider the same

APA material properties and wing design as previously discussed, but allow for the maximum free strain of the APA be increased. Fig. 30 shows the impact on wing twist distribution along the outer wingspan for different levels of APA's free strain. Considering the case of 3.75-fold increase in free strain (and keeping the passive material properties of the APA the same), Fig. 31 show the impact on roll rate and roll angle responses. As indicated in these plots, this is the level of material improvement required so the wing-warping concept may achieve similar levels of performance as the aileron concept discussed before. These levels were improvements may be theoretically achievable[12] but only time can tell the viability of the concept.
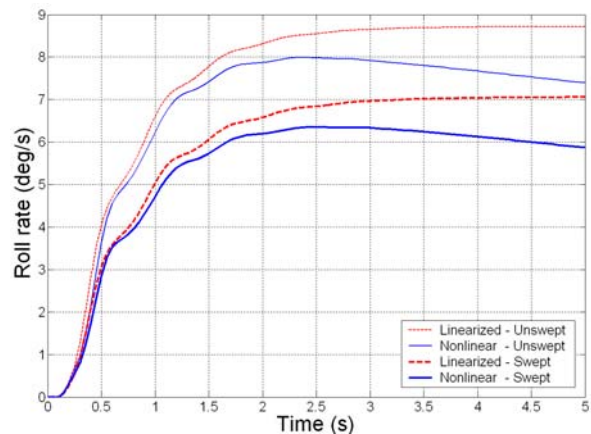

Figure 28: Active concept roll response for different outer wing sweep angles (25° sweep indicated by "Swept"; flight index 5, maximum actuation).
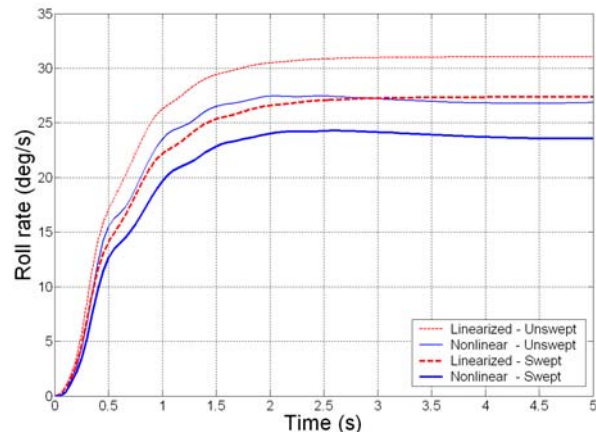

Figure 29: Aileron concept roll response for different outer wing sweep angles (25° sweep indicated by "Swept"; flight index 5, maximum actuation).
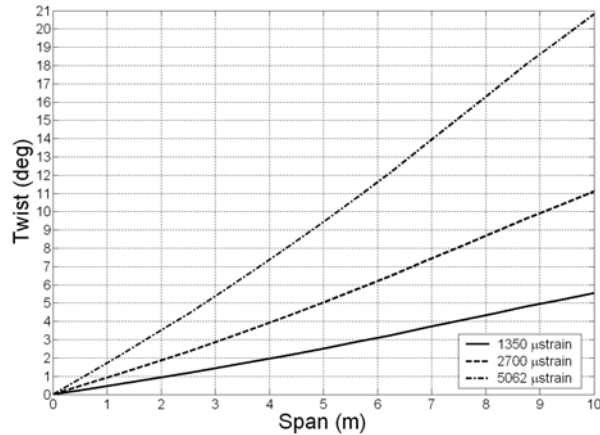
Figure 30: Spanwise twist distribution on the active outer wing considering different APA free strain levels (1350 μstrain represents available technology)

General Remarks

Even though numerical design optimization will improve the baseline vehicle designs and should be employed support navigating such reach design space, the relative results obtained here represent the order of response expected from each concept for the joined-wing Sensorcraft configuration. Again, the concepts are based on current technology material properties and construction practices. The active concept uses APA properties that are achievable with today's technology and the model includes all the fundamental static and dynamic effects on the aeroelastic responses. The aileron design contains significant idealizations, and represents the performance upper bound for the concept. No surface control inertia or aerodynamic losses with high deflection angles have been included in the model, or any control flexibility that comes with very large control surfaces. In fact, the chosen size of the aileron was based on the maximum practical size surface that can be fitted within such wing[11] without being concerned with mechanical fixtures and actuator systems.

Another important aspect of the vehicles' designs presented here is that they are driven by strength consideration, which penalized the wing-warping concept and favored the aileron-actuated one. Stiffness constraints got automatically satisfied once the layups were thickened enough to sustain the high loads. If a reduced maximum load factor is chosen, other constraints may become active, particularly related to aileron reversal and gust loads (as was seen for the latter in some of the design studies conducted in Ref. 5). In fact, the overall system/mission requirements, including performance and survivability considerations, will certainly impact the design solution, potentially changing the importance of roll performance as assumed here.
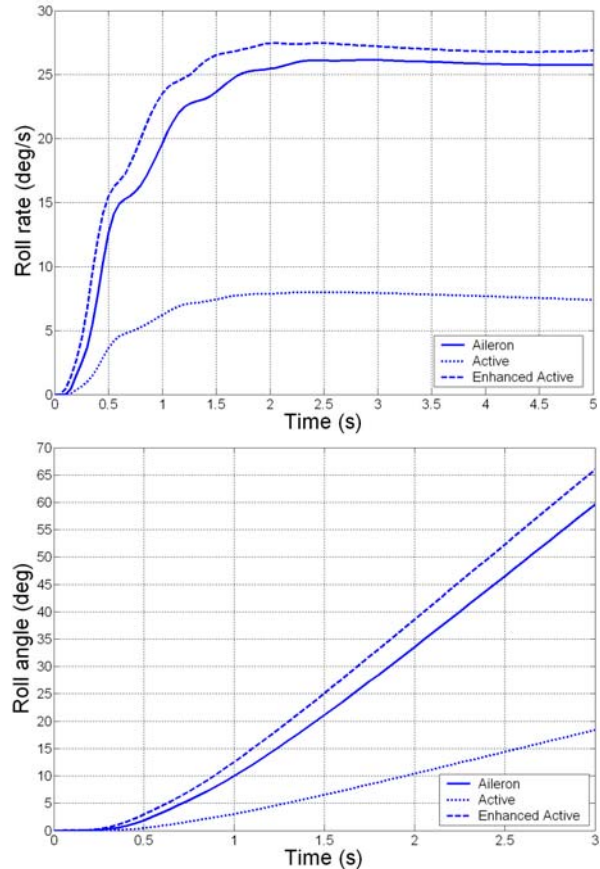

Figure 31: Roll response considering a mechanically equivalent APA but with 3.75-fold increase in its free strain properties (flight index 5; vehicles are trimmed prior to roll maneuver)

Conclusions

This paper discussed some of the unique aeroelastic characteristics of the joined-wing Sensorcraft, with emphasis on the concept of wing warping actuation for maneuver load generation. The study employs a newly developed framework for the analysis, design, and simulation of high-flexible multi-segmented wing vehicles, also described in this paper.

To study the effectiveness of wing warping to generate aircraft roll control, two baseline vehicles were designed. The first one has anisotropic piezocomposite actuators embedded in the composite construction of the outer wing, inducing strain and twist deformation. The second baseline vehicle has an aileron spanning 50% of the outer wing. Both designs satisfy the same set of constraints. Strength of the laminates at 2.5-g load factor became the sizing constraint for both designs.

When analyzing the joined-wing concepts, the importance of wing flexibility and the availability of a

geometrically nonlinear structural dynamics solver were demonstrated. Of particular interest for the joined-wing configuration is the criticality of the sudden rear wing loss of stiffness (buckling) that compromises the vehicle integrity. For the roll response, it was shown that the wing-warping design based on currently APA technology presents a terminal roll rate which is over three-times smaller than the aileron concept due to limited twist authority. This could be overcome with an APA of similar mechanical properties as used in this study but with 3.75-times greater maximum free strain. This is within range of the promises of single-crystal fiber composites.

Acknowledgements

References

[1] Pendleton, E. W., Griffin, K. E., Kehoe, M., and Perry, B., "A Flight Research Program for the Active Aeroelastic Wing Concept," In *Proceedings of the 37th AIAA/ASME/AHS/ASC Structures, Structural Dynamics and Materials Conference*, Salt Lake City, Utah, April 1996.

[2] Bent, A. A., "Active Fiber Composite Material Systems for Structural Control Applications," In *Proceedings of the SPIE's 6th International Symposium on Smart Structures and Materials,* Newport Beach, California, March 1999.

[3] Wilkie, W.K., Bryant, R.G., High, J.W., Fox, R.L., Hellbaum, R.F., Jalink, A., Little, B.D., and Mirick, P.H., "Low-cost piezocomposite actuator for structural control applications," In *Proceedings of the SPIE 7th Sympsosium on Smart Structures and Materials,* Newport Beach, California, March 2000. pp. 323-334.

[4] Cesnik, C. E. S. and Ortega-Morales, M., "Active Aeroelastic Tailoring of Slender Flexible Wings," *International Forum on Aeroelasticity and Structural Dynamics*, Madrid, Spain, June 5—7, 2001.

[5] Brown, E. L., "Integrated Strain Actuation in Aircraft with Highly Flexible Composite Wings," Ph.D. Thesis, Massachusetts Institute of Technology, Cambridge, Massachusetts, June 2003.

[6] Livne, E., "Aeroelasticity of Joined-Wing Airplane Configurations: Past Work and Future Challenges - A Survey," In *Proceedings of the 42nd AIAA/ASME/AHS/ ASC Structures, Structural Dynamics, and Materials Conference*, Seattle, WA, April 16-19, 2001, AIAA-2001-1370.

[7] Blair, M. and Canfield, R. A., "A Joined-Wing Structural Weight Modeling Study," In *Proceedings of the 43rd AIAA/ASME/AHS/ASC Structures, Structural Dynamics and Materials Conference*, Denver, Colorado, April 2002, AIAA-2002-1337.

[8] Roberts, R. W., Canfield, R. A., and Blair, M., "Sensor-craft Structural Optimization and Analytical Certification," In *Proceedings of the 44th AIAA/ASME/AHS/ASC Structures, Structural Dynamics and Materials Conference*, Denver, Colorado, April 2003.

[9] Reich, G. W., Raveh, D., and Zink, P. S., "Application of Active Aeroelastic Wing Technology to a Joined-Wing Sensorcraft," In *Proceedings of the 43rd AIAA/ASME/AHS/ASC Structures, Structural Dynamics and Materials Conference*, Denver, Colorado, April 2002, AIAA-2002-1633.

[10] Peters, D. A. and Johnson, M. J., "Finite-State Airloads for Deformable Airfoils on Fixed and Rotating Wings", In *Symposium on Aeroelasticity and Fluid/Structure Interaction, Proceedings of the Winter Annual Meeting*. ASME, November 6 -11, 1994.

[11] Ikegami, R., Private communication, The Boeing Co., Phantom Works, Seattle, Washington, 2002.

[12] Rossetti Jr., G. A., Pizzochero. A., and Bent, A. A., "Recent Advances in Active Fiber Composites Technology," In *Proceedings of the* 12th IEEE International Symposium on Applications of Ferroelectrics, Honolulu, Hawaii, 2000, pp. 753-756.